On the Numerical Simulation of Wave-Plasma Interactions in Electrodeless Plasma Thrusters

IEPC-2025-328

Presented at the 39th International Electric Propulsion Conference, Imperial College London, London, United Kingdom
14-19 September 2025

Hugo Bergerioux * and Mario Merino†
Department of Aerospace Engineering, Universidad Carlos III de Madrid, Leganés, 28911, Spain

We investigate the occurrence of fine oscillatory wave structures in Electron Cyclotron Resonance Thruster simulations, observed in regions with resonance cones and whose nature — physical or numerical — remains ambiguous. To this end, we build a rigorous verification framework for cold plasma numerical full-wave simulations. We first derive an analytical solution to a generalized anisotropic Fresnel problem. Then, we reformulate our in-house finite element wave solver, implementing a custom waveguide port boundary condition compatible with anisotropic plasmas, enabling direct comparison with the analytical model. Guided by a numerical dispersion analysis, the vector wave equation is discretized using mixed Nédélec–Lagrange finite elements. This framework enables to confirm the numerical origin of observed oscillatory patterns and their connection to resonance cones, typically in regions III, VII and VIII of the CMA diagram. Several mitigation techniques are tested, with varying success in reducing these spurious solutions. Combined with a convergence study across different element types, these results show that a structured rectangular mesh offer the most effective strategy in this planar homogeneous configuration. This work provides a preliminary foundation for understanding and mitigating spurious modes in wave-plasma simulations, offering insights for developing efficient, flexible, and physically reliable wave solvers for fully coupled particle/fluid–wave Electrodeless Plasma Thruster simulations.

I. Introduction

Electrodeless Plasma Thrusters (EPTs) are electric propulsion devices that generate and accelerate plasma using externally applied electromagnetic fields,[1,2] eliminating the need for neutralizers or exposed electrodes. These systems rely on the absorption of electromagnetic waves to heat electrons, which then drive ionization and acceleration. In particular, Electron-Cyclotron Resonance Thrusters (ECRTs) use resonant microwave absorption, through waveguide[3–5] or coaxial[6,7] coupling. Accurately modeling the propagation and absorption of these waves within the plasma is therefore essential to understanding the physical processes at play, optimizing power deposition, and guiding the design and performance estimation of such thrusters.

Within the Equipo de Propulsión Espacial y Plasmas (EP2) group, the hybrid PIC-fluid code HYPHEN-EPT has been developed to simulate plasma discharge, incorporating a two-dimensional, full-wave model.[8–10] This wave code solves Maxwell's equations in the 2D axisymmetric discharge chamber in the frequency domain using a mixed Nédélec-Lagrange finite element (FE) discretization, and describes the linearized plasma response to electromagnetic fields through the cold plasma approximation. This approach is widely used to study wave propagation in plasmas, capturing the essential wave–plasma interaction mechanisms.

However, persistent challenges can arise in wave regimes where principal resonances, or more ubiquitously, resonance cones, appear. In these parametric propagation regions, very small wavelength waves are allowed by the planar-wave dispersion relation, indicating that a fine discretization is needed to correctly simulate them. Indeed, recent simulations[11] of the EP2 waveguide ECRT prototype provided insights into the energy

*Ph.D. Student, hbergeri@ing.uc3m.es.
†Full professor, mario.merino@uc3m.es.

Copyright 2025 by the Electric Rocket Propulsion Society. All rights reserved.

deposition and plasma loss mechanisms, but also revealed patterns of rapidly oscillating fields in regions where resonance cones exist, as observed in Fig. (1). These small structures, which occur predominantly in the neighborhood of the transition from the waveguide to the plasma, were found to be close to the mesh size, raising the question of their numerical accuracy.

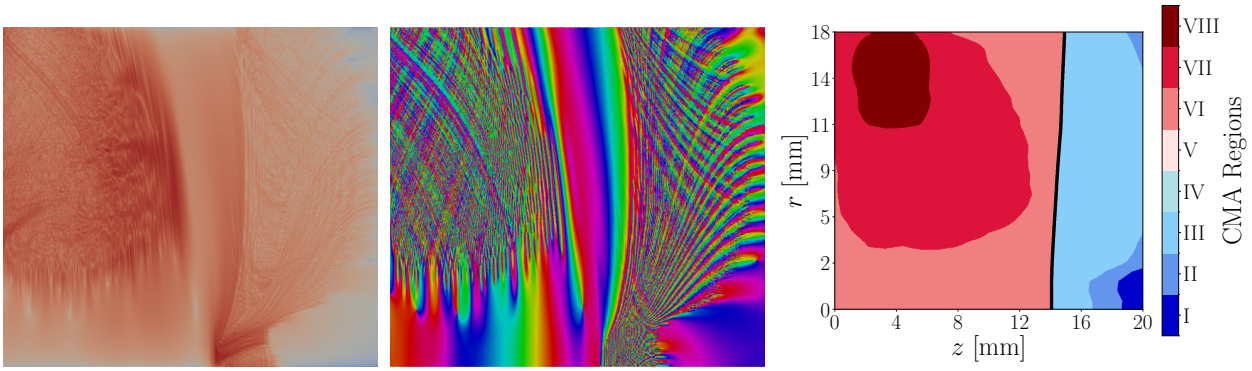

(a) $|E_z|$ **(b)** φ_z **(c) Regions of CMA diagram.**

Figure 1: Magnitude and phase of the z-component of the electric field E_z — in the meridian plane of the axisymmetric plasma discharge chamber — from previous ECRT simulations with radial injection and azimuthal mode $m = +1$. The corresponding regions of the CMA diagram are mapped onto the same domain in Fig. (1c), with the resonance (solid black line) separating regions VI and III. Fig. (1a) and Fig. (1b) taken from 11.

Indeed, a preliminary analysis based on mesh refinement did not show these structures to converge within the range explored, unless extraordinary damping (i.e. dissipation due to collisions) is added to the model. Although their impact on power deposition appears limited,[11] resolving this uncertainty is essential for improving simulation accuracy and advancing our understanding of wave–plasma interactions in EPTs. More broadly, this highlights the critical need for rigorous verification procedures in wave–plasma solvers, a step often overlooked but vital to ensuring model fidelity and predictive capability.

To address these challenges, in this work we first reformulate and re-implement the cold plasma wave solver, developing a more flexible version in the Julia computing language based on the Gridap library.[12,13] After introducing the cold plasma model in section II, we discuss the FE discretization of the wave equation in section III, with particular attention to the choice of elements and basis functions. To quantify the impact of these choices, we conduct a numerical dispersion analysis, systematically characterizing numerical errors and spurious solutions that may arise. Crucially, to assess the physical relevance of these numerical artifacts, we turn to a well-posed verification case with an analytical solution in section IV : the generalized Fresnel problem of a plane wave traveling from a semi-infinite vacuum to a semi-infinite, uniform magnetoplasma. This generalization of the classical (i.e. isotropic) Fresnel problem which we present is not found in the literature to the best of our knowledge, and provides an ideal analytic benchmark to study the accuracy and convergence of different numerical schemes under a sharp medium transition, for multiple incidence angles and wave-plasma propagation conditions, varying the plasma density, magnetic field strength, and direction. To work out our study, we also incorporate a custom waveguide port boundary condition compatible with the plasma anisotropic medium. This enables a direct comparison of analytical and numerical results across different discretizations and plasma configurations, shedding light on the circumstances under which spurious solutions appear, and exploring strategies to mitigate them.

II. Cold plasma dielectric model

The cold plasma model provides a simplified yet physically meaningful description of wave propagation in magnetized plasmas. It relies on several assumptions : a collisionless, non-relativistic, and low-temperature plasma, where thermal motion is neglected and only the collective response of electrons and ions to electromagnetic fields is considered. The model arises from the linearization of the macroscopic momentum equation in the cold fluid limit—neglecting forces related to divergence of pressure tensor—and assuming

Copyright 2025 by the Electric Rocket Propulsion Society. All rights reserved.

time-harmonic perturbations around a stationary equilibrium. The plasma response is therefore encapsulated in a frequency-dependent anisotropic dielectric tensor $\overline{\overline{\kappa}}$. This model is widely presented in the plasma physics literature[14–16] and enables the coupling of Maxwell's equations with plasma dynamics. Considering Maxwell's equations (without source term) with time-harmonic fields $\boldsymbol{E}(\boldsymbol{r},t) = \mathrm{Re}[\hat{\boldsymbol{E}}(\boldsymbol{r})\exp(-i\omega t)]$, where ω is the angular frequency, $\hat{\boldsymbol{E}}$ the complex amplitude of the field, and using the Fourier transform in time $\partial/\partial t \to -i\omega$, one gets a formulation of the curl-curl wave equation :

$$\nabla \times (\nabla \times \hat{\boldsymbol{E}}) - \frac{\omega^2}{c^2}\overline{\overline{\kappa}}\hat{\boldsymbol{E}} = \boldsymbol{0}, \tag{1}$$

where the tensor $\overline{\overline{\kappa}}$ is defined such that the electric displacement field becomes $\boldsymbol{D} = \overline{\overline{\varepsilon}}\boldsymbol{E} = \varepsilon_0\overline{\overline{\kappa}}\boldsymbol{E}$. Considering the convention of a magnetic field along the z-axis,[14] the cold plasma dielectric tensor is defined as :

$$\overline{\overline{\kappa}} = \begin{pmatrix} S & -iD & 0 \\ iD & S & 0 \\ 0 & 0 & P \end{pmatrix}, \tag{2}$$

where

$$S = \frac{R+L}{2}, \quad D = \frac{R-L}{2}, \tag{3}$$

$$R = 1 - \frac{\omega_{pe}^2}{\omega\left[(\omega + i\nu_e) - \omega_{ce}\right]}, \quad L = 1 - \frac{\omega_{pe}^2}{\omega\left[(\omega + i\nu_e) + \omega_{ce}\right]}, \quad P = 1 - \frac{\omega_{pe}^2}{\omega\left(\omega + i\nu_e\right)}, \tag{4}$$

with $\omega_{pe} = \sqrt{ne^2/(m_e\varepsilon_0)}$ the plasma frequency and $\omega_{ce} = eB/m_e$ the electron cyclotron frequency. In the high-frequency range, the ion contribution to the induced plasma current is much lower than the one of electrons, and thus can be neglected.

In infinite homogeneous plasmas, equation Eq. (1) admits planar wave solutions :

$$\boldsymbol{E}(\boldsymbol{r},t) = \tilde{\boldsymbol{E}}\exp\left[i(\boldsymbol{k}\cdot\boldsymbol{r} - \omega t)\right], \tag{5}$$

with $\tilde{\boldsymbol{E}}$ a new complex amplitude that captures both the harmonic time and space variations of the field. If we apply now the transformation on the curl operator $\nabla \times \boldsymbol{E} \to i\boldsymbol{k} \times \boldsymbol{E}$, Eq. (1) becomes :

$$\boldsymbol{k} \times \left(\boldsymbol{k} \times \tilde{\boldsymbol{E}}\right) + \frac{\omega^2}{c^2}\overline{\overline{\kappa}}\tilde{\boldsymbol{E}} = 0. \tag{6}$$

The dispersion relation in Eq. (6) can also be written as a function of the norm of the refractive index vector $\boldsymbol{n} = (c/\omega)\boldsymbol{k}$ and the propagation angle θ, such that $\boldsymbol{n} = n\cos(\theta)\hat{\mathbf{e}}_z + n\sin(\theta)\hat{\mathbf{e}}_x$:

$$\tan^2\theta = -\frac{P\left(n^2 - R\right)\left(n^2 - L\right)}{\left(Sn^2 - RL\right)\left(n^2 - P\right)}. \tag{7}$$

This formulation helps to define cutoffs — when the wave-vector vanishes, and propagating modes become evanescent — and resonances : in the absence of collisional damping, critical transitions occur at the singularity $n \to \infty$, and energy can be strongly absorbed. These phenomena are closely related to the plasma and cyclotron frequencies of the constituent species. Within the literature on cold plasma model, the Clemmow-Mullaly-Allis (CMA) diagram provides a valuable graphical tool for classifying wave propagation regimes, mapping regions of propagation, cutoff, and resonance in terms of normalized plasma and cyclotron frequencies. In fact, in some regions of the CMA diagram, the propagation is strongly affected by resonance and has been shown both theoretically and experimentally to give rise to resonance cones,[15,17] so-called because $n \to \infty$ at a given propagation angle θ_c with respect to the magnetic field. Indeed, taking this limit in the dispersion relation formulation from Eq. (7), one obtains the resonant condition on the wave propagation angle :

$$\tan^2(\theta_c) = \lim_{n\to\infty}\tan^2(\theta) = -\frac{P}{S}, \tag{8}$$

so that when the critical value θ_c is approached, shorter wavelength propagate, and beyond θ_c all waves become evanescent. Therefore, in addition to identifying critical cutoffs and resonance surfaces, the CMA diagram also delineates distinct wave regimes, including regions where resonance cones can form due to strong anisotropy in the plasma response. It offers clear insight into the dispersive and directional behavior of waves in magnetized plasmas across varying frequency and magnetic-field conditions. In this work, we will refer to different regions of the CMA diagram—specifically regions I and VIII, following nomenclature from 14–16—to explore distinct wave phenomena in different plasma regimes.

Copyright 2025 by the Electric Rocket Propulsion Society. All rights reserved.

III. Mixed finite element discretization

To investigate the propagation of electromagnetic waves in a magnetized plasma, Maxwell's equations are solved in the frequency domain using the cold plasma model introduced previously. However, solving Eq. (1) in realistic geometries and under relevant boundary conditions requires a robust numerical framework. We therefore introduce a FEM wave solver, specifically developed for this study, which enables full-wave simulations of the electric field in two-dimensional domains. The FEM is a widely used technique for solving partial differential equations (PDE), particularly well-suited for problems involving complex boundaries and heterogeneous media, as it is the case in plasma–wave interaction studies. Moreover, there is evidence that FEM outperforms FD methods in this context,[10,18] especially by mitigating spurious noise near resonant regions, which are critical features in plasma–wave interactions.

The development of this solver builds upon previous work within the EP2 group,[8–10] in particular the electromagnetic module of the HYPHEN-EPT hybrid PIC-fluid code, which implements a similar frequency-domain, full-wave model using the cold plasma approximation. In the present study, we re-implement and extend this numerical model in the Julia programming language, using the FE library Gridap. This new implementation preserves the physical foundations of the original model, while offering enhanced modularity and flexibility for defining custom boundary conditions and material regions.

A. Numerical discretization

1. *Variational formulation*

The FEM is based on a variational formulation of the governing wave equation Eq. (1). For this, the PDE is first multiplied by a test function $\boldsymbol{T}$ and integrated over the simulation domain Ω :

$$\int_\Omega \left[\nabla \times \left(\nabla \times \hat{\boldsymbol{E}}\right)\right] \cdot \hat{\boldsymbol{T}}^* \, \mathrm{d}\Omega - k_0^2 \int_\Omega \overline{\overline{\kappa}} \hat{\boldsymbol{E}} \cdot \hat{\boldsymbol{T}}^* \, \mathrm{d}\Omega = 0, \tag{9}$$

with $k_0 = \omega/c$. The unknown electric field is approximated using a trial function expanded over a finite set of basis functions, while the test function drawn from the same function space is used to weight the residual of the equation. When test and trial functions are chosen from the same basis, this procedure is known as the Galerkin method. The first term in Eq. (9) can be developed using integration by parts. The appearing boundary term is simplified using Gauss's theorem, resulting in the weak formulation :

$$\int_\Omega \left[\left(\nabla \times \hat{\boldsymbol{T}}^*\right) \cdot \left(\nabla \times \hat{\boldsymbol{E}}\right) - k_0^2 \overline{\overline{\kappa}} \hat{\boldsymbol{E}} \cdot \hat{\boldsymbol{T}}^*\right] \, \mathrm{d}\Omega + \oint_{\partial\Omega} \left[\hat{\boldsymbol{n}} \times (\nabla \times \hat{\boldsymbol{E}})\right] \cdot \hat{\boldsymbol{T}}^* \, \mathrm{d}S = 0, \tag{10}$$

with $\hat{\boldsymbol{n}}$ the normal unit vector to the boundary pointing outward. The FE discretization transforms the weak form into a linear system, whose unknowns are the degrees-of-freedom (DOFs) of the electric field in the mesh.

This weak form can then be applied to different cases to study wave propagation in 2D domains (2D3V). Here, a planar case of the wave problem is implemented, which is used to obtain the numerical results presented in section IV. The wave propagation is fully planar, which impacts the definition of the curl operator : derivatives with respect to y are null. To solve cylindrical problems in a 2D domain characterized by axial direction z and radial direction r, a Fourier expansion of the time harmonic complex amplitudes is taken in the periodic $\hat{\mathbf{e}}_\theta$ direction :

$$\hat{\boldsymbol{E}}(r, \theta, z) = \sum_{m=-\infty}^{\infty} \boldsymbol{E}^{(m)}(r, z) \exp(im\theta), \tag{11}$$

with m the azimuthal Fourier mode number. The curl operator needs to be carefully handled in this case, rewriting the differential operator as $\nabla \rightarrow (-\nabla_\mathrm{t}(im/r)\hat{\mathbf{e}}_\theta)$, with ∇_t the in-plane differential operator used in the planar case. By solving each of the considered modes independently and summing the results, the full 3D solution is reconstructed efficiently (generally far faster than a direct 3D computation), taking advantage of the system linearity.

Copyright 2025 by the Electric Rocket Propulsion Society. All rights reserved.

2. Anisotropic waveguide port absorbing boundary condition

To accurately simulate wave injection in anisotropic media in the planar case while preventing artificial reflections (for the analysis in section IV), we develop a new custom boundary condition that acts both as a wave launcher and an absorbing boundary. This allows us to introduce waves of prescribed amplitude and polarization into the domain and ensure that outgoing (reflected) waves are effectively absorbed. Such a setup is essential to enable meaningful comparison with analytical solutions, but it can also be used in cylindrical geometry for ECRT simulations. In classical electromagnetic problems the development of such port boundary conditions for vacuum waveguides[19,20] relies on the orthogonality of waveguide modes to project and separate modal components, greatly simplifying the formulation. However, in anisotropic media such as magnetized cold plasma, wave polarizations are generally non-orthogonal. Consequently, the formulation of a waveguide port boundary condition is nontrivial and requires a careful reformulation to properly handle this more general case.

The boundary condition aims to correctly represent the term $\hat{\boldsymbol{n}} \times (\nabla \times \hat{\boldsymbol{E}})$ from Eq. (10), defined on the left and right boundaries from the domain in the analysis of section IV. Assuming a modal decomposition of the total field, both the incident and reflected fields are expanded as a sum over the linearly independent wave polarizations :

$$\begin{cases} \hat{\boldsymbol{E}}^{\text{in}} = \sum_n A_n^{\text{in}} \boldsymbol{P}_n^{\text{in}} \exp(ik_{z,n}^{\text{in}} z), \\ \hat{\boldsymbol{E}}^{\text{re}} = \sum_n A_n^{\text{re}} \boldsymbol{P}_n^{\text{re}} \exp(ik_{z,n}^{\text{re}} z), \end{cases} \tag{12}$$

with n the number of incident (and thus reflected) modes. The boundary integrand $\hat{\boldsymbol{n}} \times (\nabla \times \hat{\boldsymbol{E}})$ is then computed for both incident and reflected fields. The incident modes, of amplitude A_n^{in}, are fully prescribed, whereas the reflected mode amplitudes A_n^{re} are the unknowns to be determined. For this, the reflected field is expressed as $\hat{\boldsymbol{E}}^{\text{re}} = \hat{\boldsymbol{E}} - \hat{\boldsymbol{E}}^{\text{in}}$, and then projected on each of the reflected modes $\boldsymbol{P}_m^{\text{re}}$ over the boundary surface :

$$\oint_{\partial\Omega} \boldsymbol{P}_m^{\text{re}} \cdot \hat{\boldsymbol{E}}^{\text{re}} \, \mathrm{d}S = \oint_{\partial\Omega} \boldsymbol{P}_m^{\text{re}} \cdot \hat{\boldsymbol{E}} \, \mathrm{d}S - \oint_{\partial\Omega} \boldsymbol{P}_m^{\text{re}} \cdot \hat{\boldsymbol{E}}^{\text{in}} \, \mathrm{d}S, \tag{13}$$

yielding a linear system for the unknown reflected amplitudes A_n^{re}. These integrals can be specifically written as :

$$\begin{cases} \oint_{\partial\Omega} \boldsymbol{P}_m^{\text{re}} \cdot \hat{\boldsymbol{E}}^{\text{re}} \, \mathrm{d}S = M_{mn}^{\text{re}} A_n^{\text{re}}, \\ \oint_{\partial\Omega} \boldsymbol{P}_m^{\text{re}} \cdot \hat{\boldsymbol{E}}^{\text{in}} \, \mathrm{d}S = M_{mn}^{\text{in}} A_n^{\text{in}}, \end{cases} \tag{14}$$

where matrices M^{re} and M^{in} capture the projections of the different polarization vectors. Notice that if the modes are orthogonal the matrix M_{mn}^{re} is simply diagonal, since off-diagonal terms capture the anisotropy of the problem here. Solving the system yields the amplitudes :

$$A_n^{\text{re}} = M_{mn}^{\text{re}^{-1}} \left[\oint_{\partial\Omega} \boldsymbol{P}_m^{\text{re}} \cdot \hat{\boldsymbol{E}} \, \mathrm{d}S - M_{mn}^{\text{in}} A_n^{\text{in}} \right], \tag{15}$$

providing a closure to the analytical definition of the boundary integral. Practically, this is implemented through computation of the DOFs of the finite element basis functions, and of the different modal fields over the boundary. Following nomenclature from 19 the $\hat{\boldsymbol{n}} \times (\nabla \times \hat{\boldsymbol{E}})$ term in the weak form split into a trial-dependent term $\boldsymbol{P}(\hat{\boldsymbol{E}})$, added to the bilinear form, and a known source $\boldsymbol{U}^{\text{in}}$, included in the linear form. This construction results in a boundary condition that naturally absorbs outgoing waves and injects the correct incident field, even in the presence of anisotropy and mode coupling. While introduced here for boundary matching in semi-infinite magnetoplasma, the proposed infrastructure also provides a general framework for classical waveguide applications, including the excitation of specific modes in vacuum for ECRT axisymmetric simulations.

B. Mixed finite elements

1. Lagrange finite elements

In the FE framework, Lagrange nodal elements are among the most widely used basis functions for spatial discretization. They are constructed from simple nodal shape functions L_i, namely Lagrange polynomials whose DOFs correspond to the field values at the mesh nodes. This construction ensures interpolation of

Copyright 2025 by the Electric Rocket Propulsion Society. All rights reserved.

the solution at nodal points and yields an $H^1(\Omega)$ conforming basis of functions. Owing to their simplicity, flexibility, and well-established theoretical properties, Lagrange elements are a natural choice for a broad class of problems. However they are not always suitable for electromagnetic problems. In particular, when applied to the vector wave equation, their $H^1(\Omega)$ conformity may lead to non-physical solutions.

Indeed, a fundamental aspect of discretizing Maxwell's equations lies in respecting the functional analytic structure of the underlying continuous problem. Maxwell's curl–curl operator in Eq. (9) acts naturally in the space $H(\mathrm{curl}, \Omega)$, within a chain of nested spaces connected by the gradient, curl, and divergence operators. This chain is known as the de Rham sequence[21,22] and can be written as :

$$\mathbb{R} \longrightarrow H^1(\Omega) \xrightarrow{\nabla} H(\mathrm{curl}, \Omega) \xrightarrow{\nabla\times} H(\mathrm{div}, \Omega) \xrightarrow{\nabla\cdot} L^2(\Omega) \longrightarrow 0. \tag{16}$$

A key property of this sequence is its exactness, meaning that the image of each operator coincides with the kernel of the next, ensuring the proper Helmholtz decomposition of vector fields. When constructing FE spaces, it is essential to replicate this sequence discretely. The canonical choice is the discrete de Rham complex :

$$V_h^0 \xrightarrow{\nabla} V_h^1 \xrightarrow{\nabla\mathrm{x}} V_h^2 \xrightarrow{\nabla\cdot} V_h^3, \tag{17}$$

where V_h^0 is a Lagrange nodal space for scalars, V_h^1 is a Nédélec edge space for $H(\mathrm{curl})$, V_h^2 is a Raviart-Thomas space for $H(\mathrm{div})$, and V_h^3 consists of discontinuous piecewise constants. In a conforming discretization (like Nédélec edge elements), the discrete kernel exactly matches the gradients of the discrete scalar space. This discrete exactness prevents the creation of spurious kernels of the curl–curl operator.[22]

However if one attempts to discretize the vector wave equation with nodal vector elements, as Lagrange elements, the discrete de Rham sequence is broken : the image of the discrete gradient is not contained in the discrete kernel of the curl. This means that the nullspace of the curl–curl operator is artificially enlarged, leading to non-physical "gradient-like" eigenmodes that pollute the numerical spectrum. Such numerical solutions therefore satisfy the discrete system but not Maxwell's equations, and thus do not represent any physical electromagnetic field. These spurious modes manifest, for instance, as additional dispersion branches in eigenvalue analyses that do not correspond to physical propagating solutions. This phenomenon is observed later in this section through a dispersion analysis of the vector wave equation.

2. *Nédélec finite elements*

Nédélec edge elements[23,24] are a class of finite elements specifically designed for electromagnetic problems. They form an $H(\mathrm{curl}, \Omega)$ conforming space, with first order basis functions defined on edges rather than nodes and represented by vector fields. This construction enforces tangential continuity across element interfaces, thereby addressing a fundamental challenge in electromagnetic simulations : ensuring that fields satisfy Maxwell's equations at material interfaces, where the tangential components of electric and magnetic fields must be continuous.

As explained previously, this curl-conforming property of Nédélec elements ensures improved convergence when solving Maxwell's equations,[21,22] inherently preventing nonphysical solutions.[25] Consequently, Nédélec elements are particularly well suited for the discretization of vector wave equations[26] such as Eq. (10), and are widely used to model wave propagation and resonance in complex geometries, including fields near singularities.[27] This capability is especially important in EPTs applications, and in particular in ECRTs, where waves typically propagate from a waveguide through vacuum and dielectric walls into the plasma chamber. These configurations involve sharp transitions between media with fundamentally different properties, including anisotropic dielectric tensors in the plasma. By enforcing tangential continuity while allowing normal discontinuities, Nédélec elements provide a consistent representation of such interfaces, ensuring reliable modeling of wave transmission and absorption. Nevertheless, the coupling among the components of the $\boldsymbol{E}$ vector due to a full dielectric tensor $\overline{\overline{\kappa}}$ complicate the analysis, and may still result in numerical instabilities.

3. *Mixed formulation*

In the present wave solver, the electromagnetic field is decomposed into in-plane and out-of-plane components, with either a planar or cylindrical geometry. A purely Nédélec discretization is not suitable for this setting, since extending the Nédélec space to include the out-of-plane component would require lifting the formulation into a full three-dimensional vector space $\mathbb{R}^3$, which is computationally inefficient and unnecessary for the

Copyright 2025 by the Electric Rocket Propulsion Society. All rights reserved.

reduced geometry. Instead, a mixed-element strategy is adopted. The in-plane vector components live in the propagation plane and are subject to the curl operator. They must therefore be discretized in a curl-conforming space, such as the Nédélec element space V_h^1, to respect the discrete de Rham structure. By contrast, the out-of-plane component behaves effectively as a scalar in the 2D formulation, being acted upon by gradients but not by in-plane curls. In the cylindrical formulation, the azimuthal direction is periodic and the dielectric tensor is assumed uniform along this coordinate. It can therefore be discretised consistently with a Lagrange space V_h^0 without breaking the discrete sequence.

This mixed choice preserves the mathematical structure of the de Rham complex in reduced dimension, while also yielding a computationally efficient scheme. Such hybrid approaches have proven effective in avoiding spurious noise and non-physical modes that typically arise in all-nodal implementations.[28] In our case, this strategy also builds on previous in-house developments,[8–10] which have demonstrated the robustness and accuracy of the mixed Nédélec-Lagrange formulation for plasma wave simulations. More generally, this flexibility allows the solver to handle both Cartesian planar configurations and cylindrical axisymmetric configurations within a unified framework, thereby extending its applicability to a wide range of plasma-wave interaction problems.

Now that the discretization framework is established, the next key decision concerns the choice of element shape. In this work, two main shapes — whose efficiency has been demonstrated in previous studies[29] — are considered : triangular elements, arranged in an hexagonal pattern, and structured rectangular elements. The corresponding reference elements and local mesh arrangements are represented in Fig. (2), together with the associated basis functions, as well as the conventions adopted for the numbering and orientation of global nodes and edges.

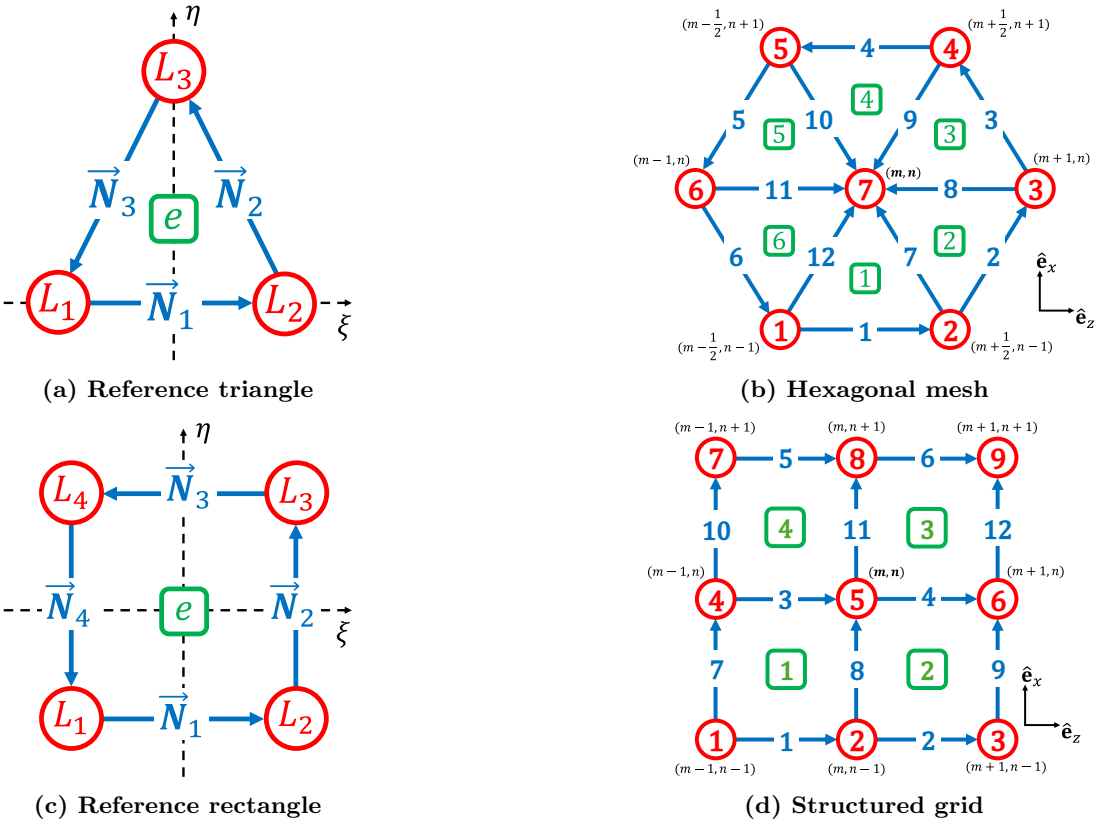

(a) Reference triangle

(b) Hexagonal mesh

(c) Reference rectangle

(d) Structured grid

Figure 2: First order triangular and rectangular mixed elements geometry and degrees of freedom. On the reference elements, Lagrange basis functions L_i are defined on the nodes, and the Nédélec basis functions $\boldsymbol{N}_i$ are associated to edges. Both global numbering conventions are illustrated : nodes are shown in red, edges in blue, and elements in green. These conventions will be consistently used in the dispersion analysis to clearly distinguish between local (element-wise) and global (mesh-wise) degrees of freedom.

Copyright 2025 by the Electric Rocket Propulsion Society. All rights reserved.

In this work, the following nomenclature is used for mixed Nédélec-Lagrange elements : T^n and R^n respectively represent mixed triangular and rectangular elements of order n. The order of a finite element refers to the polynomial degree of its basis functions. Low-order elements are simple and efficient but may require finer meshes to capture wave behavior accurately, whereas higher-order elements provide greater accuracy for smooth fields and reduce numerical dispersion, but at the cost of increased computational effort.

C. Dispersion analysis

The goal of this analysis is to study the dispersive properties of FE semi-discretizations of the two-dimensional vector wave equation. This approach builds on the development from previous studies on 2D[29] and 3D[30] FEM dispersion analysis for the scalar wave equation. Here it is extended to vector fields, with the addition of anisotropic properties characteristic of cold plasma.

In this study, we focus on the spatial discretization of the 2D planar vector wave equation in a cold plasma. The analysis is conducted here only on rectangular elements, but the procedure is similar for triangular ones, and will be completed in the future. The dispersion analysis then allows to assess how accurately the numerical scheme reproduces wave propagation by comparing the discrete dispersion relation to the analytical continuous one Eq. (6).

1. Shape functions

The first step consists in defining the basis shape functions for both full-Lagrange and mixed Nédélec-Lagrange descriptions. In FEM, shape functions are used to locally approximate the solution within each element, forming the building blocks for constructing the global solution over the entire mesh.

LAGRANGE Let's define the local coordinates $(\xi, \eta) \in [-1, 1] \times [-1, 1]$, and consider the numbering from Fig. (2c). First order Lagrange shape functions L_i, corresponding to node i of coordinates (ξ_i, η_i), should equal 1 at node i and 0 at all other nodes : $L_i(\xi_j, \eta_j) = \delta_{ij}$. The general bilinear shape functions are :

$$L_i(\xi, \eta) = \frac{1}{4} (1 + \xi\, \xi_i) (1 + \eta\, \eta_i) . \tag{18}$$

NÉDÉLEC First order Nédélec shape functions $\boldsymbol{N}_j$, corresponding to edge j, should fulfill the following properties : the integral of their tangential component equals 1 along edge j, and 0 along all the other edges. Considering the edges orientation in Fig. (2c), the shape function for each edge is :

$$\boldsymbol{N}_1(\xi, \eta) = \frac{1 - \eta}{2}\, \hat{\mathbf{e}}_\xi, \quad \boldsymbol{N}_2(\xi, \eta) = \frac{1 + \xi}{2}\, \hat{\mathbf{e}}_\eta, \quad \boldsymbol{N}_3(\xi, \eta) = -\frac{1 + \eta}{2}\, \hat{\mathbf{e}}_\xi, \quad \boldsymbol{N}_4(\xi, \eta) = -\frac{1 - \xi}{2}\, \hat{\mathbf{e}}_\eta. \tag{19}$$

FIELDS DISCRETIZATION The first configuration considered in the dispersion analysis is the full Lagrange discretization. In this approach, the three components of the fields are approximated by Lagrange elements. Considering the reference rectangular element in Fig. (2c), each component is discretized with 4 DOFs :

$$\hat{E}_x(z, x) = \hat{E}^e_{x,i} L_i(z, x), \quad \hat{E}_y(z, x) = \hat{E}^e_{y,i} L_i(z, x), \quad \hat{E}_z(z, x) = \hat{E}^e_{z,i} L_i(z, x), \tag{20}$$

with $\hat{E}^e_{x,i}$, $\hat{E}^e_{y,i}$ and $\hat{E}^e_{z,i}$ the nodal values of each of the components at the four nodes of the elements, representing 12 local DOFs. Note that the summation over repeated indices is implied.

In the second case, corresponding to the mixed-element discretization, the out-of-plane component $\hat{E}_y$ is approximated with Lagrange elements, whereas the in-plane components $\hat{E}_x$ and $\hat{E}_z$ are discretized with Nédélec edge elements :

$$\hat{E}_y(z, x) = \hat{E}^e_{y,i} L_i(z, x) \quad \text{and} \quad \begin{pmatrix} \hat{E}_z(z, x) \\ \hat{E}_x(z, x) \end{pmatrix} = \hat{E}_{zx,i} \boldsymbol{N}_i(z, x), \tag{21}$$

with $\hat{E}_{zx,i}$ the edge values of the in-plane component at the four edges.

Consequently, representing both in-plane components within the reference Nédélec rectangular element requires only 4 DOFs, compared to 8 for a Lagrange element. Including the out-of-plane component, the mixed formulation thus totals 8 local DOFs per reference element.

Copyright 2025 by the Electric Rocket Propulsion Society. All rights reserved.

Let's define the local vector of DOFs as $\boldsymbol{u}^e$, which gathers the DOFs of all components within a reference element, and the global vector of DOFs $\boldsymbol{u}$, assembled from the contributions of the four elements of the mesh. For the Lagrange discretization, this mesh has 9 nodes, leading to 27 global DOFs. In contrast, the mixed discretization involves 9 DOFs for the out-of-plane component and 12 for the in-plane components (associated with the 12 edges), yielding a total of 21.

2. *Mass and stiffness matrices*

From this point onward, the mathematical procedure is identical for both cases. The local DOFs vector $\boldsymbol{u}^e$ is related to the global one $\boldsymbol{u}$ by Boolean connectivity matrices B^e :

$$u_i^e = B_{ij}^e u_i. \tag{22}$$

These connectivity matrices define, for each of the four elements in Fig. (2d), the mapping between the local numbering and orientation of nodes and edges (as given in the reference element) and their global counterparts in the mesh. By substituting Eq. (20) or Eq. (21), depending on the discretization considered, together with Eq. (22) into the weak formulation without boundary terms, Eq. (10), we obtain the discretized weak form :

$$K_{ij}u_j - k_0^2 M_{ij}u_j = 0, \tag{23}$$

with $M_{ij} = \sum_e B_{ki}^e m_{kl}^e B_{lj}^e$ and $K_{ij} = \sum_e B_{ki}^e k_{kl}^e B_{lj}^e$ respectively the global mass and stiffness matrices, constructed from the local mass and stiffness matrices, obtained by integration over the reference element.

3. *Dispersion relations*

Now we consider the regular mesh shown in Fig. (2d), with horizontal and vertical spacings Δz and Δx, respectively. The discrete solution on this mesh can then be expressed in the form of a plane wave :

$$\boldsymbol{u}_{m,n} = \begin{pmatrix} A_x \\ A_y \\ A_z \end{pmatrix} \exp\left(ik_z m\Delta z + ik_x n\Delta x\right), \tag{24}$$

with A_x, A_y, A_z the amplitudes of the field components, and $m, n \in \{-1, 0, 1\}$. Substituting this expression into Eq. (23) yields a system that can be written as a matrix acting on the amplitude vector. The numerical dispersion relation is then obtained by enforcing the determinant of this matrix to vanish, for both the full Lagrange and mixed formulations. This dispersion relation can then be directly compared to the analytical one derived from Eq. (6), and the corresponding results are presented in the following section.

4. *Results*

Example results of this analysis are presented in Fig. (3) for the special case of propagation in vacuum, for both numerical and analytical dispersion relations. As a reminder, this corresponds here to the planar case of the problem, where the out-of-plane component of the normalized wave-vector n_y is 0.

Fig. (3a) and Fig. (3b) represent the normalized wave-vector components n_x as a function of n_z in a cartesian plot. On a discrete grid with spacing h, the Nyquist limit $k_N = \pi/h$ is the highest wavenumber that can be uniquely resolved. The phenomenon of aliasing occurs when a mode with $|k| > k_N$ is sampled, becoming indistinguishable from a lower-wavenumber mode inside the folding box : $k \in [-\pi/h, \pi/h]$, or with the normalized values $n \in [-\pi, \pi]$ here. This is why numerical dispersion relations are plotted here only in this interval, as it contains the unique, non-aliased wave information.

The black line is the analytical solution, and the red line is the numerical solution for equal horizontal and vertical grid spacings $h = \Delta z = \Delta x = c/\omega$. The appearance of additional non-physical dispersion branches in Fig. (3a) can be interpreted as a direct consequence of violating the discrete de Rham sequence. By adopting a mixed edge–nodal formulation that respects the underlying sequence, these spurious modes are eliminated in Fig. (3b), and the discrete spectrum recovers the correct physical dispersion relations.

While cartesian plots help to highlight here the presence of spurious solutions in the full Lagrange discretization, the polar plots Fig. (3c) and Fig. (3d) help to analyze the behavior of the solution in more detail, removing the areas without data. They represent the norm of the normalized wave vector, corresponding to the refraction index, in the radial direction, as a function of the propagation angle θ.

Copyright 2025 by the Electric Rocket Propulsion Society. All rights reserved.

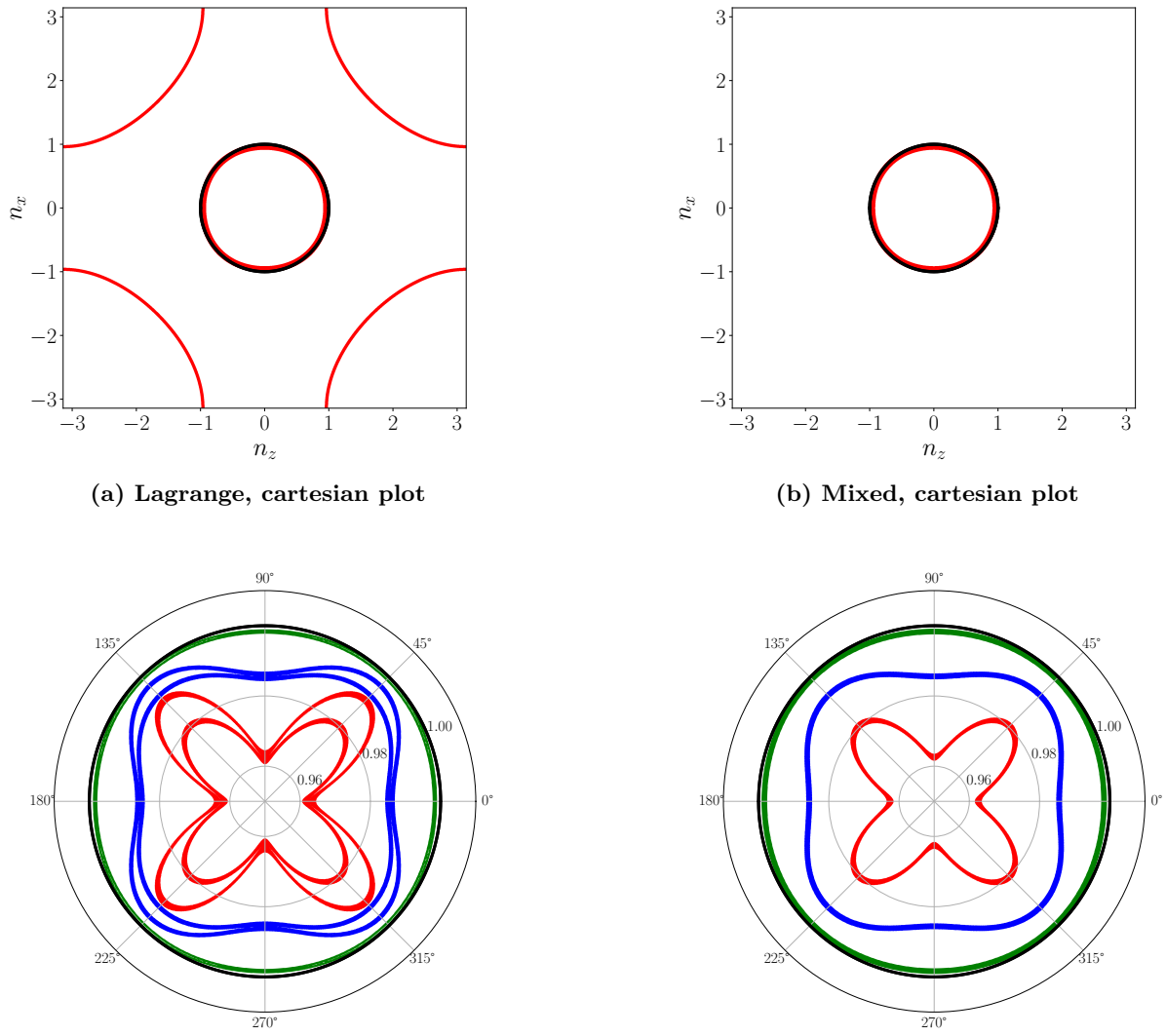

(a) Lagrange, cartesian plot

(b) Mixed, cartesian plot

(c) Lagrange, polar plot

(d) Mixed, polar plot

Figure 3: Dispersion analysis results of rectangular finite elements in vacuum. Black lines denote the analytical solution of the dispersion relation, while colored lines show numerical results : red, blue and green correspond to mesh sizes $\Delta z = \Delta x = c/\omega$, $0.6\,c/\omega$ and $0.2\,c/\omega$, respectively. Cartesian plots show the relation between the in-plane components n_x and n_z of the normalized wave vector, whereas polar plots present its magnitude $|\boldsymbol{n}|$ as a function of the propagation angle θ. Mind that the scale of the radial axis is clipped at 0.95.

For both discretizations, only the central circles is kept here, plotting $n \in [0.95, 1.05]$. The black line represents again the analytical solution, while the red, blue and green ones represent decreasing numerical grid spacing. As the spacing decreases, the numerical solution converges clearly towards the analytical one in both cases. However Fig. (3c) still shows spurious branches, not visible with the mixed formulation.

Moreover, the polar plots reveal variations in numerical accuracy depending on the propagation direction, highlighting a rectangular symmetry in the solution linked to the element shape. A higher accuracy can be observed along directions $\theta = \pi/2 \bmod \pi$, and this directional bias increases with larger grid spacing. While not shown here, equilateral triangular elements exhibit the same behavior : full Lagrange discretization

Copyright 2025 by the Electric Rocket Propulsion Society. All rights reserved.

generates spurious solutions, with preferred propagation directions reflecting the underlying triangular mesh symmetry. In the reminder of this work, only mixed Nédélec-Lagrange elements are therefore considered. The influence of anisotropic magnetoplasma properties — including singularities similar to those encountered in EPTs — is then examined in detail thanks to a dedicated analytical framework, developed in the following.

IV. Generalized Fresnel problem

To provide a validation of the wave solver, and — more importantly — to establish a reference framework for identifying and analyzing potential spurious solutions, an analytical solution to the generalized Fresnel problem is developed in this section. Whereas the classical Fresnel problem describes the interaction of an electromagnetic plane wave at the interface between two isotropic media, in the case of a magnetized plasma, the situation is fundamentally complicated by the plasma's anisotropic response. Within the cold plasma model, the dielectric tensor introduces coupling between field components and supports two eigenmodes whose wave vectors are generally not parallel. Assuming a uniform plasma, the interface supports two distinct solutions with different propagation directions and polarization states, unlike the vacuum side, where both polarizations propagate with a common wave vector.

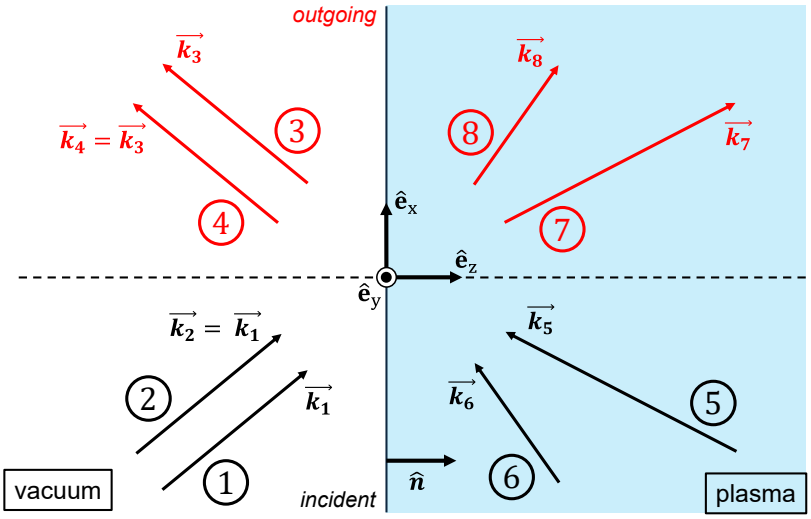

Figure 4: Sketch of the generalized Fresnel problem at the interface between vacuum and a uniform magnetized plasma. In each medium, the total field is expressed as a combination of two incident and two outgoing plane waves. The vacuum supports two incident and reflected modes corresponding to orthogonal polarizations — similarly to the classical Fresnel problem — whereas the plasma supports two eigenmodes determined by its anisotropic response.

A schematic of this generalized Fresnel problem is shown in Fig. (4). The total electromagnetic field is represented as a superposition of incoming and outgoing plane waves on each side of the interface. This formulation sets the stage for the analytical development presented below.

A. Analytical solution

We consider the general case of a fully planar electromagnetic wave problem involving eight plane waves and two uniform, anisotropic media. A linear, homogeneous, anisotropic relation is assumed for the electric displacement field, described by the tensor $\overline{\overline{\kappa}}$, and the magnetic permeability is taken to be that of vacuum, μ_0. The two media, labeled L and R, are characterized by tensors $\overline{\overline{\kappa}}_{\mathrm{L}}$ and $\overline{\overline{\kappa}}_{\mathrm{R}}$, respectively, and are separated by a planar interface located at $z = 0$. In the specific case of vacuum and cold plasma, which is the main case of study of this section, we take $\overline{\overline{\kappa}}_{\mathrm{L}} = \mathbb{I}_3$ the identity matrix and $\overline{\overline{\kappa}}_{\mathrm{R}}$ to be the cold plasma dielectric tensor, as defined in Eq. (2). To solve this problem, one needs to use the general interface conditions for electromagnetic fields. They consist of a set of four equations describing the behaviour of fields at the interface of two media, derived from the integral forms of Maxwell equations. The procedure consists in

Copyright 2025 by the Electric Rocket Propulsion Society. All rights reserved.

choosing a small square Σ across the interface, and then shrink the sides perpendicular to the interface to infinitesimal length, so that the area of integration looks like a line in this limit. In this case, they are defined as :

$$\hat{\boldsymbol{n}} \times (\boldsymbol{E}_{\mathrm{R}} - \boldsymbol{E}_{\mathrm{L}}) = \boldsymbol{0}. \tag{25}$$

$$(\boldsymbol{D}_{\mathrm{R}} - \boldsymbol{D}_{\mathrm{L}}) \cdot \hat{\boldsymbol{n}} = 0. \tag{26}$$

$$(\boldsymbol{B}_{\mathrm{R}} - \boldsymbol{B}_{\mathrm{L}}) \cdot \hat{\boldsymbol{n}} = 0. \tag{27}$$

$$\hat{\boldsymbol{n}} \times (\boldsymbol{H}_{\mathrm{R}} - \boldsymbol{H}_{\mathrm{L}}) = \boldsymbol{0}. \tag{28}$$

with $\hat{\boldsymbol{n}} = \hat{\mathbf{e}}_z$ the unit normal vector to the interface, and the eight plane waves are defined as in Eq. (5) :

$$\boldsymbol{E}_j(\boldsymbol{r}, t) = \tilde{\boldsymbol{E}}_j \exp\left[i(\boldsymbol{k}_j \cdot \boldsymbol{r} - \omega t)\right] = A_j \boldsymbol{P}_j \exp\left[i(\boldsymbol{k}_j \cdot \boldsymbol{r} - \omega t)\right], \tag{29}$$

with A_j and $\boldsymbol{P}_j$ respectively the complex amplitude and the polarization vector of the wave j. On each side of the interface, the total field can be written as a superposition of the two pairs of modes : $\boldsymbol{E}_{\mathrm{L}} = \sum_{j=1}^{4} \boldsymbol{E}_j(\boldsymbol{r}, t)$ and $\boldsymbol{E}_{\mathrm{R}} = \sum_{j=5}^{8} \boldsymbol{E}_j(\boldsymbol{r}, t)$. The interface condition on the electric field strength Eq. (25) enforces the parallel components of left and right electric fields to be equal :

$$\begin{cases} \sum_{j=1}^{4} E_{j,x} = \sum_{j=5}^{8} E_{j,x}, \\ \sum_{j=1}^{4} E_{j,y} = \sum_{j=5}^{8} E_{j,y}. \end{cases} \tag{30}$$

The second condition, on the electric displacement field Eq. (26) introduces anisotropy in the problem through the cold plasma dielectric tensor, since the displacement field in each medium is defined respectively as $\boldsymbol{D}_{\mathrm{L,R}} = \overline{\overline{\varepsilon}}_{\mathrm{L,R}} \boldsymbol{E}_{\mathrm{L,R}} = \varepsilon_0 \overline{\overline{\kappa}}_{\mathrm{L,R}} \boldsymbol{E}_{\mathrm{L,R}}$. This leads to :

$$\left(\overline{\overline{\kappa}}_{\mathrm{L}} \sum_{j=1}^{4} \boldsymbol{E}_j \right)_z = \left(\overline{\overline{\kappa}}_{\mathrm{R}} \sum_{j=5}^{8} \boldsymbol{E}_j \right)_z . \tag{31}$$

As we consider time-harmonic plane waves, we can use in Eq. (27) the relation $\boldsymbol{B} = (\boldsymbol{k} \times \boldsymbol{E})/\omega$, to replace the magnetic flux density. Therefore this interface condition gives :

$$\left(\sum_{j=1}^{4} \boldsymbol{k}_j \times \boldsymbol{E}_j \right)_z = \left(\sum_{j=5}^{8} \boldsymbol{k}_j \times \boldsymbol{E}_j \right)_z . \tag{32}$$

Finally for the condition on magnetic field strength in Eq. (28), one can use the general assumption of $\boldsymbol{B} = \mu_0 \boldsymbol{H}$, simplifying the equation to :

$$\begin{cases} \left(\sum_{j=1}^{4} \boldsymbol{k}_j \times \boldsymbol{E}_j \right)_x = \left(\sum_{j=5}^{8} \boldsymbol{k}_j \times \boldsymbol{E}_j \right)_x , \\ \left(\sum_{j=1}^{4} \boldsymbol{k}_j \times \boldsymbol{E}_j \right)_y = \left(\sum_{j=5}^{8} \boldsymbol{k}_j \times \boldsymbol{E}_j \right)_y . \end{cases} \tag{33}$$

This gives a set of 6 equations in the limit of the interface surroundings. Moreover, at an interface between two media, the tangential component of the wave vector must be continuous to ensure phase matching and satisfy the boundary conditions on the tangential components of the electromagnetic fields. In this case, it means that the parallel components k_x and k_y of all the waves considered should match. Using the general definition of the electric field in Eq. (29) together with this assumption, and recalling that the interface is set at $z = 0$, the interface conditions can be simplified by removing the exponential term, so that all the equations defined above are valid also for $\tilde{\boldsymbol{E}}_j$. The values of the wave vectors $\boldsymbol{k}_j$ are obtained separately for each medium, solving the dispersion relation Eq. (6) of the cold plasma model. From this, one can obtain the polarizations vectors $\boldsymbol{P}_j$ as eigenvectors of the problem. After some algebra, we obtain a general system valid for any pair of anisotropic uniform media, linking the amplitudes of the incident waves — prescribed by the definition of the Fresnel problem — to those of the outgoing waves, which are the unknowns.

Copyright 2025 by the Electric Rocket Propulsion Society. All rights reserved.

B. Validation of the wave solver

The goal of this section is to compare the numerical results obtained with the wave solver for a planar simulation, to the analytical solution previously derived. For this, one needs to define boundary conditions to the numerical problem so that a semi-infinite magnetoplasma can be accurately modeled. The reference simulation domain is defined as it follows : two uniform media, vacuum on the left, cold plasma on the right, separated by an interface, and the top and bottom horizontal boundaries are set as periodic conditions. For the left and right vertical walls, one needs to remove any possible wave reflection. Since the wave polarizations on each side are known a priori thanks to the analytical solution, this constraint can be artificially applied imposing a waveguide port boundary condition on those boundaries, already developed in section III. The numerical simulations are realized with a mixed discretization (following nomenclature defined in section III), using Nédélec elements for the in-plane components E_x and E_z, and Lagrange elements for the out-of-plane E_y. The incident waves considered are the two orthogonal in-plane and out-of-plane modes of a wave in vacuum (from the left side of the domain), linearly polarized, so that they correspond to the classical s- and p-polarizations, with both an equal amplitude $A_1 = A_2 = 1$. No wave is launched from plasma in this case ($A_5 = A_6 = 0$). The normalized wave number for all the waves is fixed to $n_x = 0.25$, $n_y = 0$ and n_z is found depending on the medium characteristics, through the respective dispersion relation. First we proceed to a validation of the numerical solution in a simple plasma regime. The plasma parameters are set to low densities, with plasma and cyclotron frequencies as $\omega_{pe}^2 = 0.3\omega^2$ and $\omega_{ce} = 0.3\omega$, corresponding to Region I of CMA following literature nomenclature.[14–16] For all numerical simulations of the generalized Fresnel problem presented, the magnetic field is taken as uniform and aligned with the z-axis. Additional tests with different orientations were performed, but the overall observations reported below remain unchanged, indicating that the investigated phenomena are not influenced by the magnetic field direction. The computational domain is discretized with a triangular mesh of 15k elements, generated using the Frontal-Delaunay algorithm in GMSH. Fig. (5) shows the magnitudes of the three components of the electric field for both the analytical and numerical solutions.

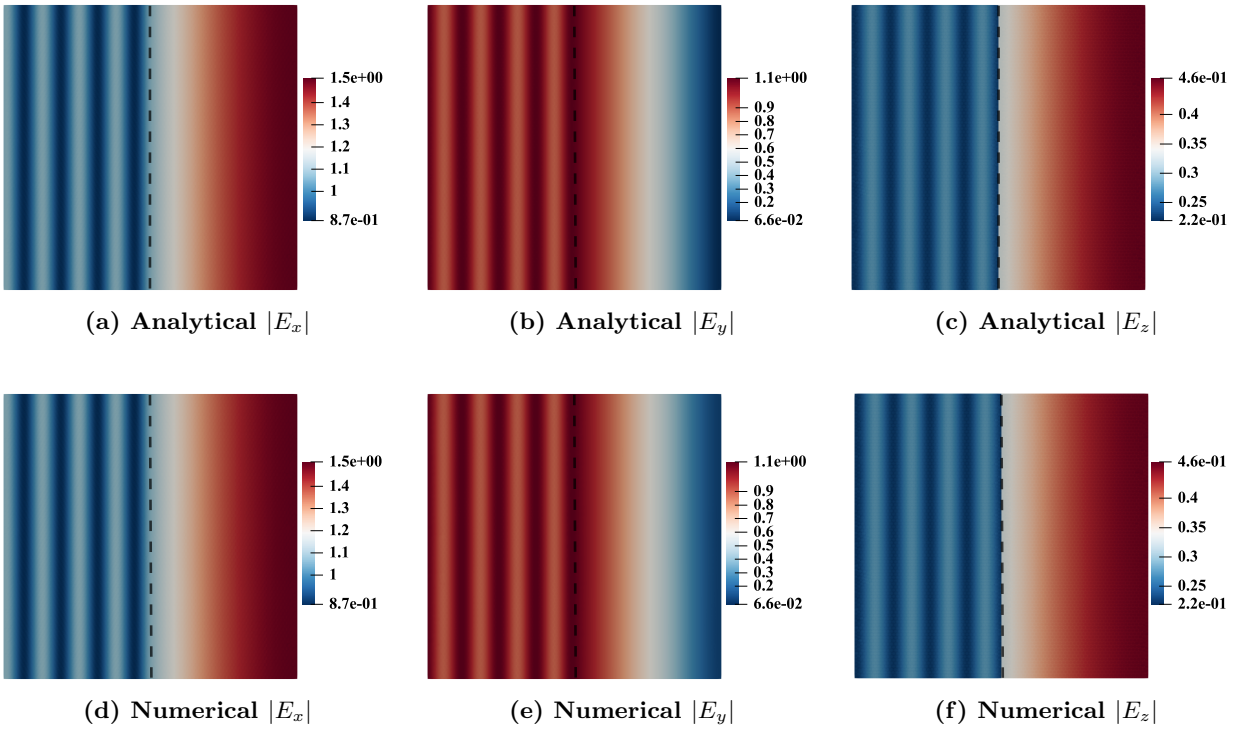

(a) Analytical $|E_x|$ **(b) Analytical $|E_y|$** **(c) Analytical $|E_z|$**

(d) Numerical $|E_x|$ **(e) Numerical $|E_y|$** **(f) Numerical $|E_z|$**

Figure 5: Comparison of numerical and analytical solutions to the generalized Fresnel problem for the magnitudes of the electric field components in CMA diagram Region I (no resonance cone). Good agreement is observed across the domain, validating both wave solver implementation and analytical development in this propagation regime. The simulation accurately captures the interaction of the wave at the vacuum–plasma interface (dark dashed line).

Copyright 2025 by the Electric Rocket Propulsion Society. All rights reserved.

In order to facilitate direct comparison, all numerical results are plotted with the same scale as the analytical ones. To obtain a complete representation of the fields, the phase results are presented in Fig. (6). They provide additional insight into the wave behavior, in particular its propagation direction and the associated phase fronts.

In this low-density plasma regime, the phase variation across the vacuum–plasma interface is relatively small, consistent with analytical predictions.

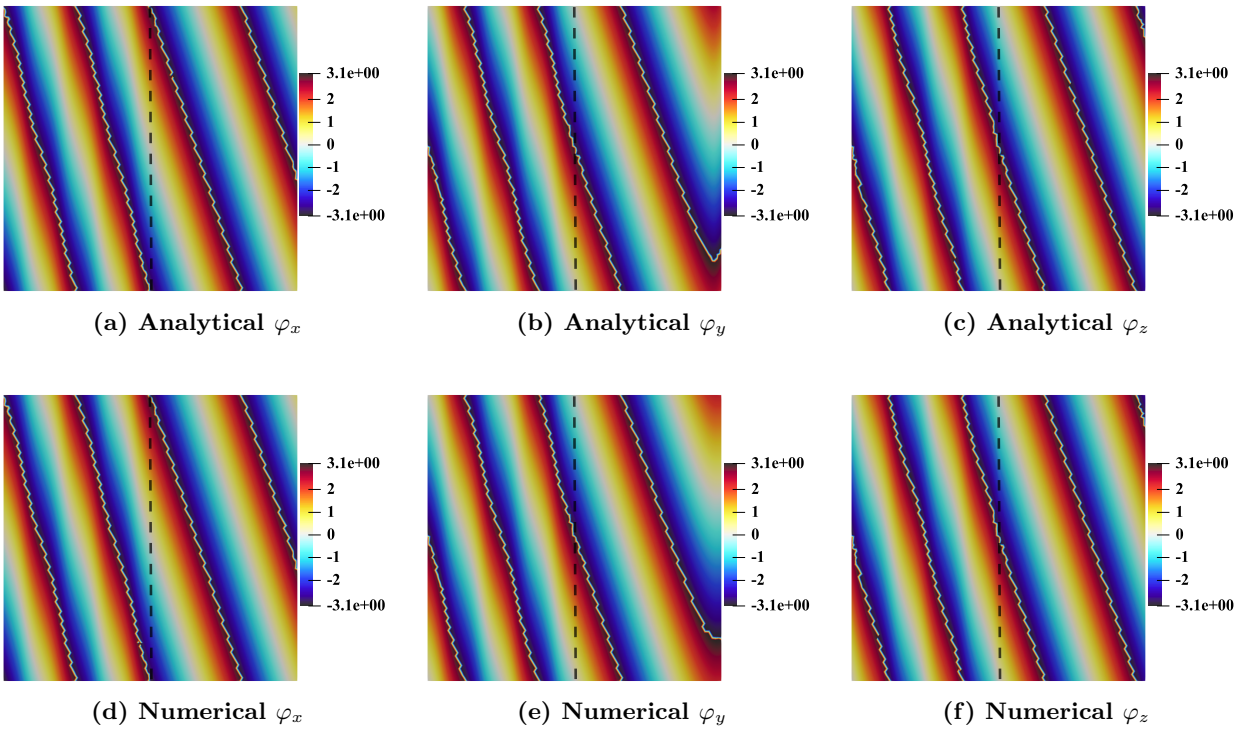

(a) Analytical φ_x **(b) Analytical φ_y** **(c) Analytical φ_z**

(d) Numerical φ_x **(e) Numerical φ_y** **(f) Numerical φ_z**

Figure 6: Comparison of numerical and analytical solutions to the generalized Fresnel problem for the phases of the electric field components in CMA diagram Region I (no resonance cone). Good agreement is observed across the domain as for the magnitudes, validating wave solver implementation and analytical development in this propagation regime.

Combined with the magnitude results, the phase plots further validate the numerical solution as both representations display close agreement with the analytical model. Results shown are for a mesh with 15k elements, confirming that the waveguide port boundary condition and the mixed discretization of the vector wave equation accurately capture the transmission and reflection phenomena at the sharp interface. This validates the wave solver for a homogeneous planar configuration.

C. Resonance cones

We now consider a cold plasma with properties corresponding to Region VIII of the CMA diagram. As explained in section II this corresponds to a regime with resonance cones, which impacts plasma and wave behavior. The main plasma parameters are here $\omega_{pe}^2 = 10\,\omega^2$ and $\omega_{ce} = 4\,\omega$, which will be in the following the reference case for Region VIII study.

The other simulation parameters (mesh, incident wave properties) are strictly the same as the previous simulations in Region I. The results for the magnitude and the phase of the z-component are plotted in Fig. (7). The analytical solutions in Fig. (7a) and Fig. (7b) are used as reference.

Copyright 2025 by the Electric Rocket Propulsion Society. All rights reserved.

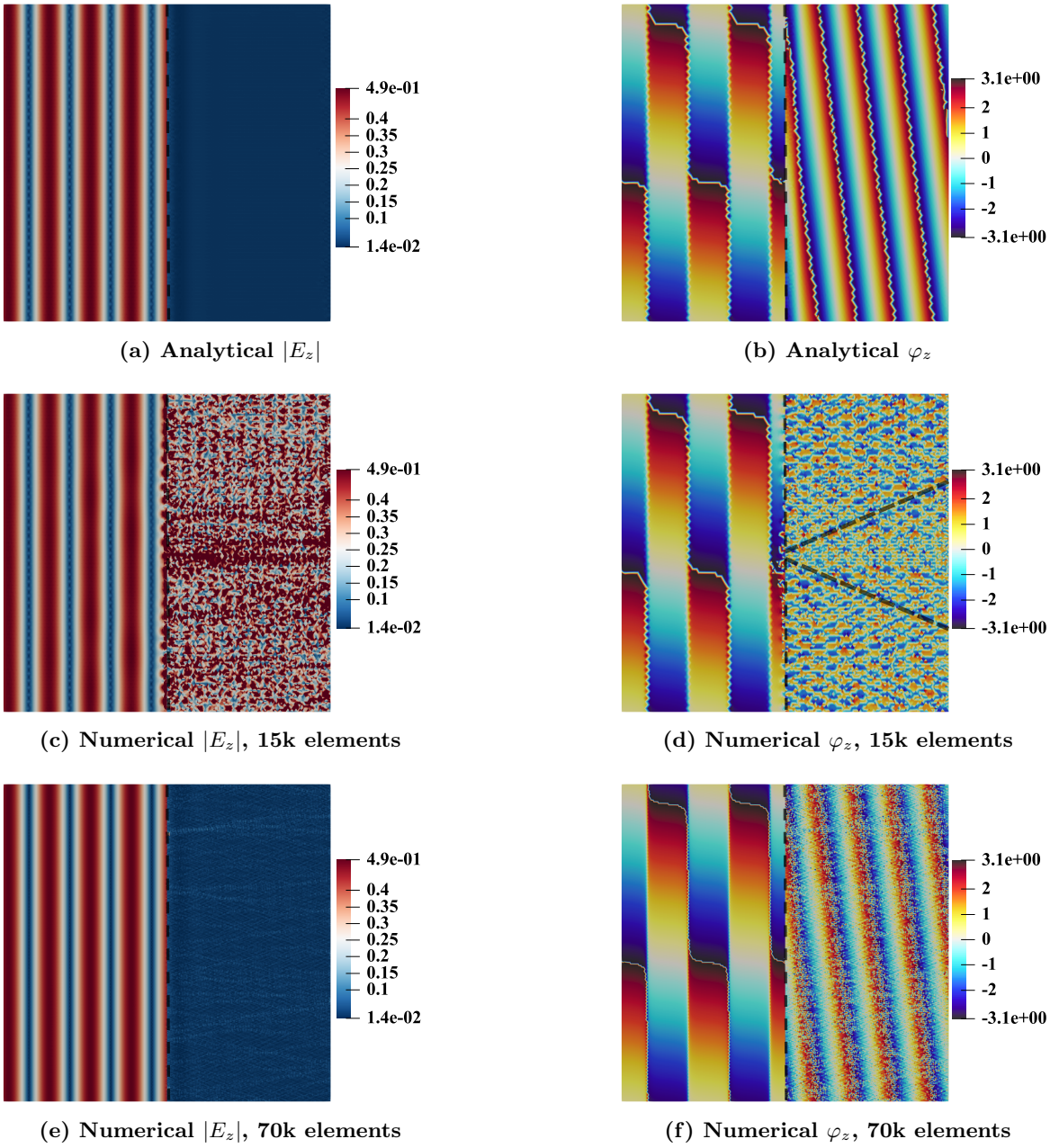

(a) Analytical $|E_z|$

(b) Analytical φ_z

(c) Numerical $|E_z|$, 15k elements

(d) Numerical φ_z, 15k elements

(e) Numerical $|E_z|$, 70k elements

(f) Numerical φ_z, 70k elements

Figure 7: Comparison of numerical and analytical solutions to the generalized Fresnel problem for the magnitude and phase of the z-component of the electric field E_z in CMA diagram Region VIII (resonance cones). Results are shown for the analytical solution and two numerical simulations using triangular meshes with approximately 15k and 70k elements. Spurious solutions appear in the numerical results, almost aligning with iso-phase surfaces (plotted in dashed dark lines in Fig. (7d), perpendicular to the resonance directions). Increasing mesh resolution reduces these spurious effects, but does not eliminate them completely.

The numerical simulation with a triangular mesh of 15k elements presents important spurious solutions, contrary to what is observed for Region I in Fig. (5) and Fig. (6). In FE simulations of electromagnetic waves, spurious solutions may arise as non-physical modes that satisfy the discrete formulation. The results for the x-component (not presented here) are very similar, whereas the ones in the out-of-plane direction y are much less affected.

Copyright 2025 by the Electric Rocket Propulsion Society. All rights reserved.

These spurious solutions only appear in parametric regions III, VII and VIII, i.e. in regimes with resonance cones, as it is observed in literature.[8,11] This link between spurious solutions and the resonance phenomenon is highlighted in the phase plot in Fig. (7d), where iso-phase surfaces (dashed dark lines) are aligning closely with appearing patterns from the numerical solutions. These surfaces are orthogonal to the theoretical critical propagation vectors, obtained with the resonance angle formula Eq. (8). In this uniform plasma from Region VIII, the critical angle is $\theta_c = 66.7°$. This observation is similar to the one already obtained for a full ECRT simulation,[11] and can be explained by the singular nature of the resonance cones. In the continuous system, the wavenumber diverges $|\boldsymbol{k}| \to \infty$ at the resonance angle, and the discrete mesh can only represent a finite maximum $|\boldsymbol{k}|$, producing high-k modes that follow the theoretical phase fronts. The spurious lines appear near but not exactly along the resonance direction, leading to a small angular deviation from the theoretical iso-phase surfaces Fig. (7d).

Fig. (8) presents the results of the dispersion analysis with mixed elements in a cold plasma, for Regions I and VIII. In Region VIII, resonance cones are clearly observed in Fig. (8b), as both analytical and numerical branches show an asymptotic behavior along the propagation directions defined by the critical resonance angle θ_c. As discussed earlier, the wave vector diverges to infinity at this specific angle. In contrast, no such phenomenon is present in Region I.

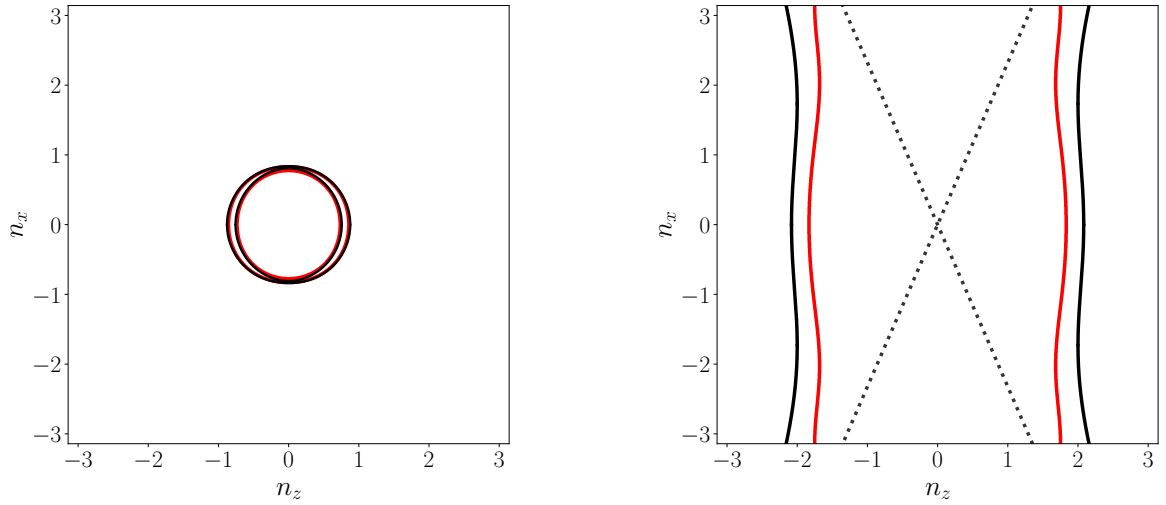

(a) Region I **(b) Region VIII**

Figure 8: Dispersion analysis results for CMA Region I and VIII. The resonance cones are clearly visible in Fig. (8b), with the branches exhibiting asymptotic behavior along resonance directions (dashed lines).

The numerical artifacts observed in the numerical solution are particularly harmful in wave–plasma interaction studies, where they can distort field structures. Mitigating them is therefore essential to ensure the physical accuracy and reliability of the wave solver.

The first approach one can think of to mitigate this problem in a FE simulation is to increase the mesh resolution. This first solution is shown in Fig. (7e) and Fig. (7f), refining the mesh to 70k elements. This approach leads to an improved solution, notably by reducing the spurious peaks observed in the magnitude. However, despite this apparent improvement, residual spurious modes remain significant, particularly evident in the phase plots when compared with the analytical solution. In addition, while the overall trend shows some improvement with an increasing number of elements, the convergence is not strictly monotonic : for instance, the results obtained with 70k elements are slightly less accurate than those with 50k elements. This phenomenon is studied in more details later in this section through a convergence study. Overall, these results lead to the need for the investigation of other, more reliable mitigation techniques.

Copyright 2025 by the Electric Rocket Propulsion Society. All rights reserved.

D. Mitigation methods

Three main methods are implemented here and results are shown in Fig. (9). The simulations are realized with 15k elements meshes, as previously. The plasma parameters remain unchanged.

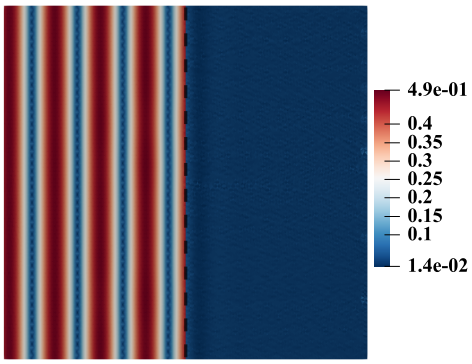

(a) $|E_z|$ with collisions, $\nu_e = 0.01\omega$

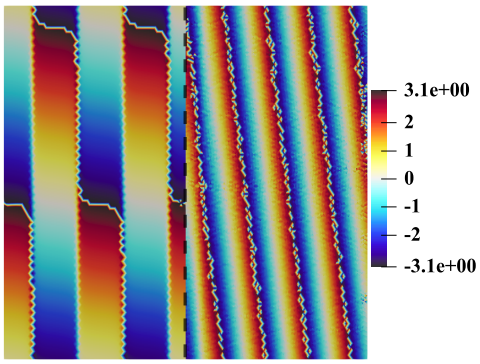

(b) φ_z with collisions, $\nu_e = 0.01\omega$

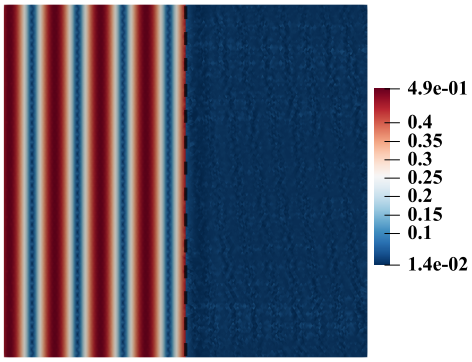

(c) $|E_z|$ order 2

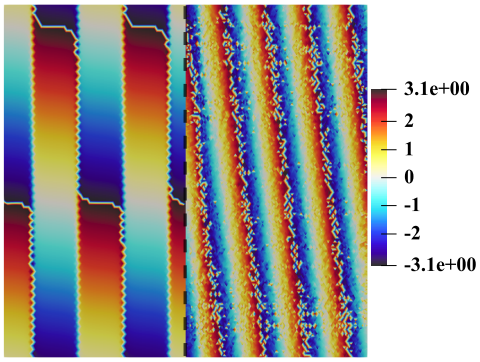

(d) φ_z order 2

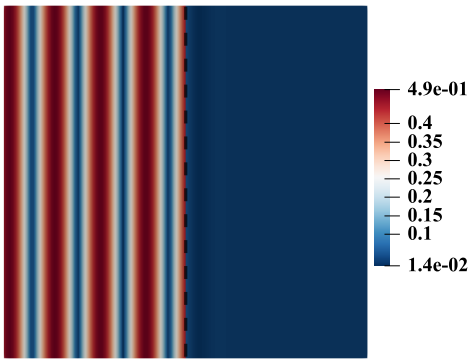

(e) $|E_z|$ with rectangular elements

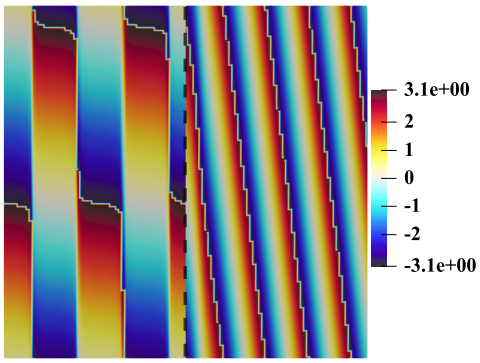

(f) φ_z with rectangular elements

Figure 9: Comparison of three mitigation techniques for the spurious solutions appearing in magnitude and phase of E_z in CMA diagram Region VIII. The methods illustrated are : adding artificial collision damping term ν_e, increasing the order of the triangular elements, and using rectangular elements. The latter not only mitigates, but completely removes spurious modes.

The first technique implies the introduction of a non-zero effective collisional term ν_e in Eq. (4). The addition of collisions eliminates singularities in the model : the refractive index does not diverge to infinite values.[18] With $\nu_e = 0.01\omega$, the spurious solutions seem sufficiently mitigated—Fig. (9a) and Fig. (9b)—although some artifacts are still visible in the phase plot. Also, this modifies the underlying physics, since it introduces artificial damping, and the choice of ν_e is not uniquely defined.

Copyright 2025 by the Electric Rocket Propulsion Society. All rights reserved.

The second technique presented in Fig. (9c) and Fig. (9d) is a usual method in FEM : increasing the order of the elements from first to second. This improves the accuracy of the solution by allowing the discretization space to better capture field variations within each element, as second order elements have more degrees of freedom. It helps increasing numerical stability by more accurately satisfying continuity constraints, leading to a more faithful representation of the physical fields. As increasing the number of elements improves slightly the solution, using one of these two first methods combined with a finer mesh give even better results, however the spurious solutions are still mitigated, and not completely removed. Going further, third order elements T^3 yield only marginal improvements, while fourth order elements T^4 eliminate spurious solutions entirely. However, the computational cost of the latter is nearly two orders of magnitude higher than that of first order triangles, making such a discretization impractical for large-scale problems that require to mesh a fine geometry with sufficient elements.

Finally, simulations with a structured grid of rectangular elements are presented in Fig. (9e) and Fig. (9f). The number of elements is the same as with triangular elements. This new shape of elements appear to completely remove spurious modes from the numerical solution, even at first order, with a good agreement with the analytical solution. Resonance cones appear to not have any effect on the results anymore. It is expected that the special conditions leading to a grid of rectangular elements to simulate correctly the waves may break down when approaching more complex problems and geometries. For now, the origin of this behavior is not fully understood and requires further numerical investigation, including a detailed comparison of dispersion results between triangular and rectangular elements.

E. Mesh convergence study

To quantitatively assess the accuracy of the numerical solution $\boldsymbol{E}_\mathrm{h}$, one can compute the L^2 norm of the error over the domain Ω. It measures the integrated difference between the computed and analytical fields :

$$||\boldsymbol{E}_\mathrm{h} - \boldsymbol{E}_\mathrm{ana}||_{L^2} = \sqrt{\int_\Omega ||\boldsymbol{E}_\mathrm{h}(\boldsymbol{r}) - \boldsymbol{E}_\mathrm{ana}(\boldsymbol{r})||^2 \, \mathrm{d}\boldsymbol{r}}. \tag{34}$$

The L^2 norm provides a standard measure of the overall error in field amplitude, making it a suitable metric for accuracy and convergence studies. To assess the performance of the wave solver, we therefore conduct a convergence study in Fig. (10) using the different mesh types and element orders presented in before.

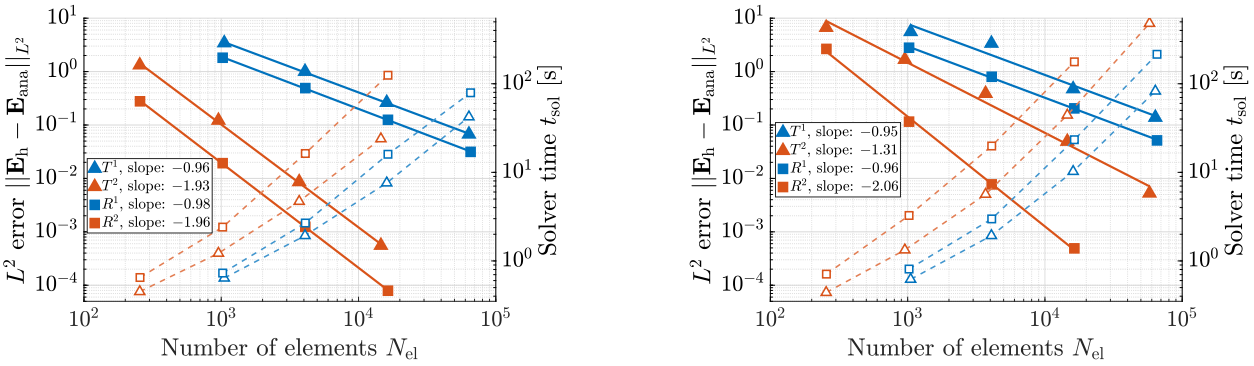

(a) Region I **(b) Region VIII**

Figure 10: Convergence study for the generalized Fresnel problem in CMA regions I and VIII, comparing different mesh types. The L^2 error with respect to the analytical solution and the solver time are shown as functions of the number of elements. The same axis scales are used for both plots to allow direct visual comparison. Triangular and rectangular elements are denoted by triangle and square markers, respectively; first-order elements are shown in blue, second-order in orange. Filled symbols indicate the L^2 error, whereas empty symbols represent solver time. The slope of the fitted error curves is printed, reflecting the observed order of convergence. In Region VIII, the presence of resonance cones leads to spurious solutions that degrade the error convergence for triangular meshes.

Copyright 2025 by the Electric Rocket Propulsion Society. All rights reserved.

Specifically, it compares mixed elements Nédélec-Lagrange, with different order and geometrical shape : first order T^1 and second order T^2 triangles, and first order R^1 and second order R^2 rectangles, by evaluating the L^2 error of the electric field solution as a function of the number of elements composing the mesh. The computational time required to assemble and solve the linear system for each case is also reported. It is important to mention that the meshes are refined for each simulation, at each step, ensuring consistent topology and element quality, allowing fair comparisons.

In Region I, as highlighted previously in this section, no anomalous behavior is observed. Both triangular and rectangular meshes converge at the expected rate, the slope of the fitted error corresponding to the order of the elements. Rectangles present a higher accuracy overall, but also higher computational needs : this is due to their intrinsic properties. As shown in section III, rectangles naturally present more degrees of freedom per element, so the observed behavior is expected.

In Region VIII however, the spurious solutions presented before influence directly the error computation for the triangles, and therefore the convergence rate. Both first and second order triangles error behavior are not linear : as mentioned in the discussion of Fig. (7), the error globally decreases with an increasing number of elements for triangular meshes, but the trend is not neat. The error exhibits an apparently irregular behavior, attributable to the presence of spurious solutions. The L^2 error does not really converge, which leads to incoherent slopes when trying to fit the data (especially for second order elements in this case). In Fig. (9e) and Fig. (9f), we saw that rectangular elements however solve completely the spurious solutions. Therefore here, both first and second order converge as expected, with respective convergence rates of 0.96 and 2.06.

When simulating cold plasmas, especially those with properties leading to regimes with resonance cones, rectangular elements appear to be the best choice in our toy Fresnel problem. In Fig. (9c) and Fig. (9d) we also saw that second and fourth order triangles help mitigating the spurious modes. In this convergence study, one can argue that they actually behave better than first order rectangles, with lower errors. However, first order rectangles present two main advantages that make them much more suitable for this kind of simulation : they are much more stable with respect to spurious solutions, as they completely eliminate them, and mostly, their computation time is much smaller. In the typical application of the wave solver, to simulate EPTs together with a plasma transport code through iterations, the computational performance of the solver is also a very important criteria.

However, the application to EPTs realistic configurations, rectangular structured grid can present one main downside : this kind of mesh is far less modular than the classical algorithm generated meshes in finite elements, in the sense that complex geometries might be harder to implement. Moreover, care must be taken in interpreting these results, as they are obtained for a planar homogeneous configuration and do not directly reflect the axisymmetric, inhomogeneous nature of practical ECRT setups.

V. Conclusion

This work aims to understand the nature of the fine wave patterns previously observed in ECRT simulations. This motivation led to the key contribution of this work : the development of an analytical solution to a generalized anisotropic Fresnel problem, which serves as a rigorous verification benchmark for assessing numerical accuracy and understanding spurious solutions. The wave solver was re-implemented in a more flexible framework, featuring a custom waveguide port boundary condition compatible with anisotropic media such as cold plasmas. This design enables a direct and accurate comparison with the analytical benchmark. This framework revealed that the oscillatory wave structures are of numerical origin — they are indeed spurious solutions — as they do not appear in the analytical solution. Nevertheless, these structures remain closely associated to resonance cone phenomena, as they are observed in specific wave propagation regimes. Importantly, we showed that adopting structured rectangular elements effectively eliminates these patterns in the case of the Fresnel problem, providing a robust and computationally efficient discretization strategy.

However, it is important to notice that this conclusion is drawn for a homogeneous plasma with simple geometry in a planar configuration. In inhomogeneous plasmas and more complex geometries, such as those encountered in realistic axisymmetric ECRT simulations, these results may not directly apply. While this work provides a clearer understanding of the conditions under which spurious solutions arise in electromagnetic wave simulations of EPT plasmas and identifies effective strategies for their mitigation, the precise mechanisms governing the emergence and suppression of spurious modes remain only partially understood.

Through a dispersion analysis of the curl–curl wave equation, we demonstrated that a full Lagrange dis-

Copyright 2025 by the Electric Rocket Propulsion Society. All rights reserved.

cretization is inherently unsuitable for the vector wave equation, whereas a mixed Nédélec–Lagrange formulation provides a consistent and physically reliable alternative, as known from the literature on FE analysis. Building on this approach, future work should extend the dispersion analysis to compare low- and high-order triangular and rectangular elements, complemented by Fourier diagnostics of localized simulation domains, to develop a more comprehensive understanding of spurious mode behavior. Further investigations could explore the impact of alternative mesh structures, such as deformed but structured quadrilateral meshes, as well as different discretizations of the vector wave equation incorporating a saddle point formulation with penalty terms.

Ultimately, this work highlights the critical importance of rigorous verification procedures in wave–plasma solvers. Looking forward, a spurious-free and computationally efficient solver opens the door to more ambitious applications. In particular, coupling the axisymmetric model (which have been already validated through the method of manufactured solutions) with the hybrid code HYPHEN for fully self-consistent particle/fluid–wave simulations of ECRTs will enable both deeper physical insight and support the optimization of next-generation thruster designs, with a particular focus on wave power deposition in the plasma.

Acknowledgments

The authors thank P. Jiménez for the insightful discussions on the previous version of the wave code, and M. R. Inchingolo for the full ECRT wave simulations in the introduction. This work has received funding from the European Research Council (ERC) under the European Union's Horizon 2020 research and innovation programme (Starting Grant ZARATHUSTRA, grant agreement N°950466).

References

[1]S. Bathgate, M. Bilek, and D. Mckenzie, "Electrodeless plasma thrusters for spacecraft: a review," *Plasma Science and Technology*, vol. 19, no. 8, p. 083001, 2017.

[2]K. Takahashi, "Helicon–type radiofrequency plasma thrusters and magnetic plasma nozzles," *Reviews of Modern Plasma Physics*, vol. 3, p. 3, 2019.

[3]S. Peterschmitt and D. Packan, "Impact of the Microwave Coupling Structure on an Electron-Cyclotron Resonance Thruster,"

[4]M. R. Inchingolo, M. Merino, and J. Navarro-Cavallé, "Plume characterization of a waveguide ecr thruster," *Journal of Applied Physics*, vol. 133, no. 11, p. 113304, 2023.

[5]M. R. Inchingolo, M. Merino, M. Wijnen, and J. Navarro-Cavallé, "Thrust measurements of a waveguide electron cyclotron resonance thruster," *Journal of Applied Physics*, vol. 135, 3 2024.

[6]J. Jarrige, P. Elias, F. Cannat, and D. Packan, "Characterization of a coaxial ecr plasma thruster," in *44th AIAA Plasmadynamics and Lasers Conference, San Diego*, 2013.

[7]V. Désangles, D. Packan, J. Jarrige, S. Peterschmitt, P. Dietz, S. Scharmann, K. Holste, and P. J. Klar, "Ecra thruster advances: 30w and 200w prototypes latest performances," *Journal of Electric Propulsion*, vol. 2, no. 1, p. 10, 2023.

[8]A. Sánchez-Villar, J. Zhou, M. Merino, and E. Ahedo, "Coupled plasma transport and electromagnetic wave simulation of an ECR thruster," *Plasma Sources Science and Technology*, vol. 30, no. 4, p. 045005, 2021.

[9]P. Jiménez, M. Merino, and E. Ahedo, "Wave propagation and absorption in a helicon plasma thruster source and its plume," *Plasma Sources Science and Technology*, vol. 31, no. 4, p. 045009, 2022.

[10]P. Jiménez, J. Zhou, J. Navarro-Cavallé, P. Fajardo, M. Merino, and E. Ahedo, "Analysis of a cusped helicon plasma thruster discharge," *Plasma Sources Science and Technology*, vol. 32, no. 10, p. 105013, 2023.

[11]M. R. Inchingolo, P. Jiménez, J. Zhou, M. Merino, and J. Navarro-Cavallé, "Simulation of the discharge and microwave-plasma coupling in a waveguide ECR thruster," in 38th *International Electric Propulsion Conference*, no. IEPC-2024-592, (Toulouse, France, June 23-28), Electric Rocket Propulsion Society, 2024.

[12]S. Badia and F. Verdugo, "Gridap: An extensible finite element toolbox in julia," *Journal of Open Source Software*, vol. 5, no. 52, p. 2520, 2020.

[13]F. Verdugo and S. Badia, "The software design of gridap: A finite element package based on the julia JIT compiler," *Computer Physics Communications*, vol. 276, p. 108341, July 2022.

[14]T. H. Stix, *Waves in plasmas*. Springer Science & Business Media, 1992.

[15]D. Swanson, *Plasma Waves, 2nd Edition*. IOP Publishing, Bristol, UK, 2003.

[16]J. Bittencourt, *Fundamentals of plasma physics*. Springer, Berlin, Germany, 2004.

[17]R. K. Fisher and R. W. Gould, "Resonance Cones in the Field Pattern of a Short Antenna in an Anisotropic Plasma," *Physical Review Letters*, vol. 22, pp. 1093–1095, May 1969.

[18]M. Merino, A. Sánchez-Villar, E. Ahedo, P. Bonoli, J. Lee, A. Ram, and J. Wright, "Wave propagation and absorption in ECR plasma thrusters," in 35th *International Electric Propulsion Conference*, no. IEPC-2017-105, (Atlanta, GA), Electric Rocket Propulsion Society, 2017.

[19]J.-M. Jin and D. J. Riley, *Finite element analysis of antennas and arrays*. John Wiley & Sons, 2009.

[20]D. M. Pozar, *Microwave engineering*. John wiley & sons, 2011.

Copyright 2025 by the Electric Rocket Propulsion Society. All rights reserved.

[21]P. Monk, *Finite element methods for Maxwell's equations*. Oxford University Press, 2003.

[22]D. Boffi, F. Brezzi, and M. Fortin, *Mixed Finite Element Methods and Applications*, vol. 44 of *Springer Series in Computational Mathematics*. Berlin, Heidelberg: Springer Berlin Heidelberg, 2013.

[23]J.-C. Nédélec, "Mixed finite elements in $\mathbb{R}^3$," *Numerische Mathematik*, vol. 35, no. 3, pp. 315–341, 1980.

[24]J.-C. Nédélec, "A new family of mixed finite elements in $\mathbb{R}^3$," *Numerische Mathematik*, vol. 50, no. 1, pp. 57–81, 1986.

[25]L. García-Castillo and M. Salazar-Palma, "Second-order nédélec tetrahedral element for computational electromagnetics," *International Journal of Numerical Modelling: Electronic Networks, Devices and Fields*, vol. 13, no. 2-3, pp. 261–287, 2000.

[26]Din Sun, J. Manges, Xingchao Yuan, and Z. Cendes, "Spurious modes in finite-element methods," *IEEE Antennas and Propagation Magazine*, vol. 37, pp. 12–24, Oct. 1995.

[27]G. Mur, "Edge elements, their advantages and their disadvantages," *IEEE Transactions on Magnetics*, vol. 30, pp. 3552–3557, Sept. 1994.

[28]A. Greenwood and J. Jin, "A novel efficient algorithm for scattering from a complex BOR using mixed finite elements and cylindrical PML," *IEEE transactions on antennas and propagation*, vol. 47, no. 4, pp. 620–629, 1999.

[29]R. Mullen and T. Belytschko, "Dispersion analysis of finite element semidiscretizations of the two-dimensional wave equation," *International Journal for Numerical Methods in Engineering*, vol. 18, pp. 11–29, Jan. 1982. Publisher: Wiley.

[30]N. N. Abboud and P. M. Pinsky, "Finite element dispersion analysis for the three-dimensional second-order scalar wave equation," *International Journal for Numerical Methods in Engineering*, vol. 35, pp. 1183–1218, Oct. 1992. Publisher: Wiley.

Copyright 2025 by the Electric Rocket Propulsion Society. All rights reserved.